Title

On-demand nanoengineering of in-plane ferroelectric topologies.

Journal

Nature Nanotechnology, 20(1)

Authors

Checa, Marti
Pant, Bharat
Puretzky, Alexander
et al.

Publication Date

2025

DOI

10.1038/s41565-024-01792-1

nature nanotechnology

Article

https://doi.org/10.1038/s41565-024-01792-1

On-demand nanoengineering of in-plane ferroelectric topologies

Received: 16 April 2024

Accepted: 19 August 2024

Marti Checa[1] ✉, Bharat Pant[2], Alexander Puretzky[1], Bogdan Dryzhakov[1], Rama K. Vasudevan[1], Yongtao Liu[1], Pravin Kavle[3,4], Arvind Dasgupta[3,4], Lane W. Martin[3,4,5], Ye Cao[2], Liam Collins[1], Stephen Jesse[1], Neus Domingo[1] & Kyle P. Kelley[1]

Hierarchical assemblies of ferroelectric nanodomains, so-called super-domains, can exhibit exotic morphologies that lead to distinct behaviours. Controlling these super-domains reliably is critical for realizing states with desired functional properties. Here we reveal the super-switching mechanism by using a biased atomic force microscopy tip, that is, the switching of the in-plane super-domains, of a model ferroelectric $Pb_{0.6}Sr_{0.4}TiO_3$. We demonstrate that the writing process is dominated by a super-domain nucleation and stabilization process. A complex scanning-probe trajectory enables on-demand formation of intricate centre-divergent, centre-convergent and flux-closure polar structures. Correlative piezoresponse force microscopy and optical spectroscopy confirm the topological nature and tunability of the emergent structures. The precise and versatile nanolithography in a ferroic material and the stability of the generated structures, also validated by phase-field modelling, suggests potential for reliable multi-state nanodevice architectures and, thereby, an alternative route for the creation of tunable topological structures for applications in neuromorphic circuits.

The drive towards miniaturization in ferroelectric materials, crucial for advancements in nanoelectronics[1,2] and neuromorphic computing[3], has led to the emergence of complex polar domain configurations[1,4–11] with new functionalities. Intricate patterns of polarization, including skyrmions[12], hopfions[7] and other topological structures, can arise naturally[13]; be created by adjusting growth conditions[12,14–18]; form through stacking of twisted freestanding layers[19]; be identified in topologically confined ferroelectric domain walls[20,21]; or be induced by local stimuli such as bias pulses[22], mechanical indentation[23,24] or heat-induced phase-transitions[25]. In turn, understanding and controlling ferroelectric polarization switching mechanisms at the nanoscale is essential for integrating these polar structures into next generation technologies, highlighting the intersection of fundamental science and practical applications.

For integration into electronic devices, it is crucial that these configurations are rapidly and efficiently manipulated—written, read and erased locally and on demand[20]. While magnetic structures[9] have been extensively studied and utilized for similar purposes[26], achieving full dynamic control over these states in ferroelectrics remains challenging[27,28]. Polar centre divergent/convergent and flux-closure domains can naturally form and have been created by application of electric fields[9,22,29]. It is known that the competition between electrostatic and elastic energies is critical for the stability of the core and domain vertices of these structures[28]. To facilitate the stabilization

---

[1]Center for Nanophase Materials Sciences, Oak Ridge National Laboratory, Oak Ridge, TN, USA. [2]Department of Materials Science and Engineering, University of Texas at Arlington, Arlington, TX, USA. [3]Department of Materials Science and Engineering, University of California Berkeley, Berkeley, CA, USA. [4]Materials Sciences Division, Lawrence Berkeley National Laboratory, Berkeley, CA, USA. [5]Departments of Materials Science and NanoEngineering, Chemistry, and Physics and Astronomy and the Rice Advanced Materials Institute, Rice University, Houston, TX, USA. ✉e-mail: checam@ornl.gov

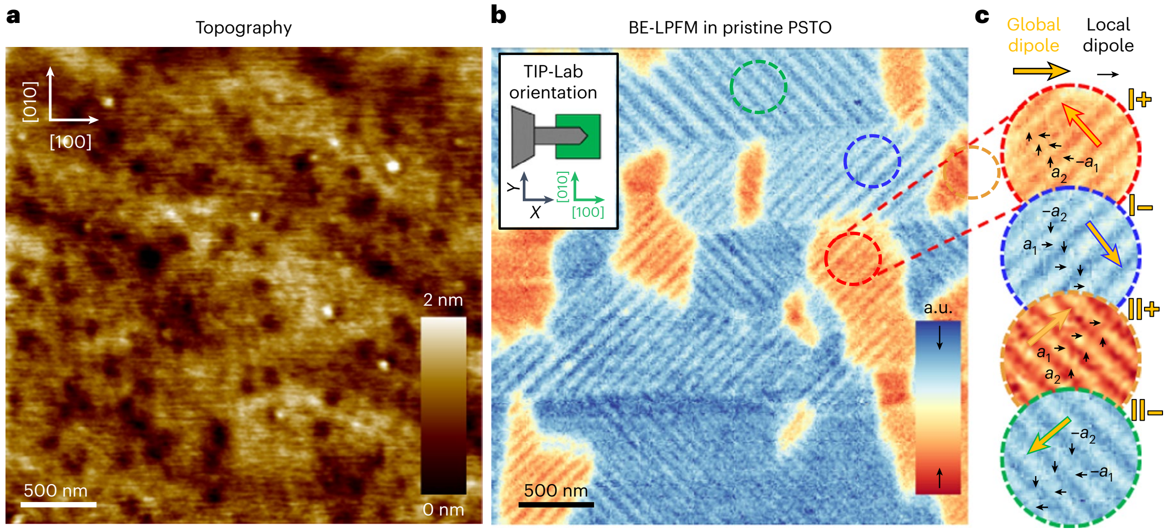

Fig. 1 | Pristine super-domain distribution in PSTO. a, The surface topography. **b**, A BE-LPFM image of the pristine sample showing the four distinct super-domain structures. The inset shows the relative TIP-laboratory orientation, the relative orientation between the cantilever of the microscope and the axes of the laboratory. **c**, The local (black) and global (yellow) dipole distribution for the four different super-domains (I+, I−, II+ and II−). The zoom-ins display examples of the four possible super-domains in the colour dashed circles in **b**.

of domains at the micro- or nano-scales, a deep understanding of local-switching mechanisms and the competing energy landscapes is required.

Using thin-film epitaxy and strain engineering, it is possible to produce ferroelectric films featuring periodic nanodomains that self-assemble into larger 'super-domains' with distinct in-plane polarization[30–32], and here, these structure serve as an ideal platform for exploring these phenomena. Prior studies have demonstrated in-plane polarization switching in these systems through the use of an atomic force microscopy (AFM)-biased tip[30], wherein it was hypothesized that the slow-scan direction produces a 'trailing' electric field responsible for driving local polarization rotation[33]. In this work, we demonstrate that the dynamics of super-domain nucleation and growth are more complex than previously reported.

Using a biased AFM tip, we performed intricate, non-standard movements along arbitrary scan paths—typically not offered by commercial scanning-probe systems—to engineer user defined effective in-plane electric fields. This approach enabled the creation of unique spiral- and flower-like tip trajectories, effectively stabilizing centre-divergent, centre-convergent and flux-closure structures in strained $Pb_{0.6}Sr_{0.4}TiO_3$ (PSTO) films. This process revealed a complex super-domain-switching mechanism (referred to as super-switching here), involving super-domain nucleation followed by stabilization of super-domain boundaries (or super-boundaries), emphasizing the critical role of the scan path's trajectory in shaping the final super-domain structure.

We have explored the complex nanoscale polarization landscape in the resulting structures regarding the ferroelectric ordering, frustration, nonlinear optics, light emission, tunability and chirality through correlative piezoresponse force microscopy (PFM), second-harmonic generation microscopy (SHG) and scanning electron microscopy cathodoluminescence (SEM-CL). Phase-field modelling validates the meta-stability of these structures, corroborating experimental data and shedding light on dipole reorganization within frustrated super-boundaries. These findings also provide a promising avenue to explore a broader range of ferroelectric topological states than previously possible by locally controlling the in-plane ferroelectric polarization on demand. By designing customized tip-trajectory configurations and integrating them in automated experiments (AE), we enable precise and versatile nanolithography patterning in ferroic materials.

Hierarchical super-switching

To explore the dynamics of super-switching, we utilized a 100 nm PSTO thin film. This model ferroelectric material, characterized by a purely in-plane polarization, is grown on a 30 nm $SrRuO_3$ electrode on a $DyScO_3$ (110) single-crystal substrate (Methods). The resulting PSTO film features a dense in-plane polarized super-domain structure[31,32] consisting of two orthogonal domain orientations (a_1 and a_2), giving rise to four distinct super-domains: II+ (a_1, a_2), II− ($-a_1$, $-a_2$), I+ ($-a_1$, a_2) and I− (a_1, $-a_2$). The global dipole of each super-domain is aligned along the crystallographic directions [110] (II+), [−1−10] (II−), [−110] (I+) and [1−10] (I−) and demarcated by distinct super-boundaries (Supplementary Fig. 1).

The surface topography and pristine distribution of super-domains is shown (Fig. 1). The net polarization direction of each super-domain is identifiable as perpendicular to the characteristic a_1/a_2 super-lattice stripes present in the lateral PFM images. To determine the polarity of the domain orientation, we have used the electrostatic convention of ref. 30.

Gaining precise control over the local in-plane ferroelectric polarization with an AFM is non-trivial, since the electric field from the biased probe in contact with the sample is primarily vertical, but it also possesses lateral components imparting a rotationally invariant applied electric field. Previous research has investigated in-plane super-switching through methods such as pulsing[9,22,34] or raster scanning[30,35] a biased tip, revealing the possiblility to stabilize single super-domains. The final polar orientation of the super-domains is determined by factors including bias polarity, sample orientation and the trajectory of the scan path[30].

To understand the microscopic origins of the super-domain formation, we performed a detailed study where the tip voltage was applied exclusively in one direction of the fast-scan motion (either trace or retrace, Fig. 2a–f), using standard raster-scan mode. Initially orienting the sample at 45° (such that the slow scan is aligned along the [110]; Fig. 2g–l), we established that (for this configuration) the slow-scan direction drives the overall polarization of the stabilized super-domain, irrespective of the fast-scan direction chosen for voltage application. In this case, it seems that the slow-scan direction drives the super-domain switching by 'pulling' the average net polarization as if it was a single domain, aligning the characteristic stripes/walls parallel to the fast-scan direction. When the sample is oriented at 0° (such that the slow scan is aligned along the [010]; Fig. 2m–r), we observed varying

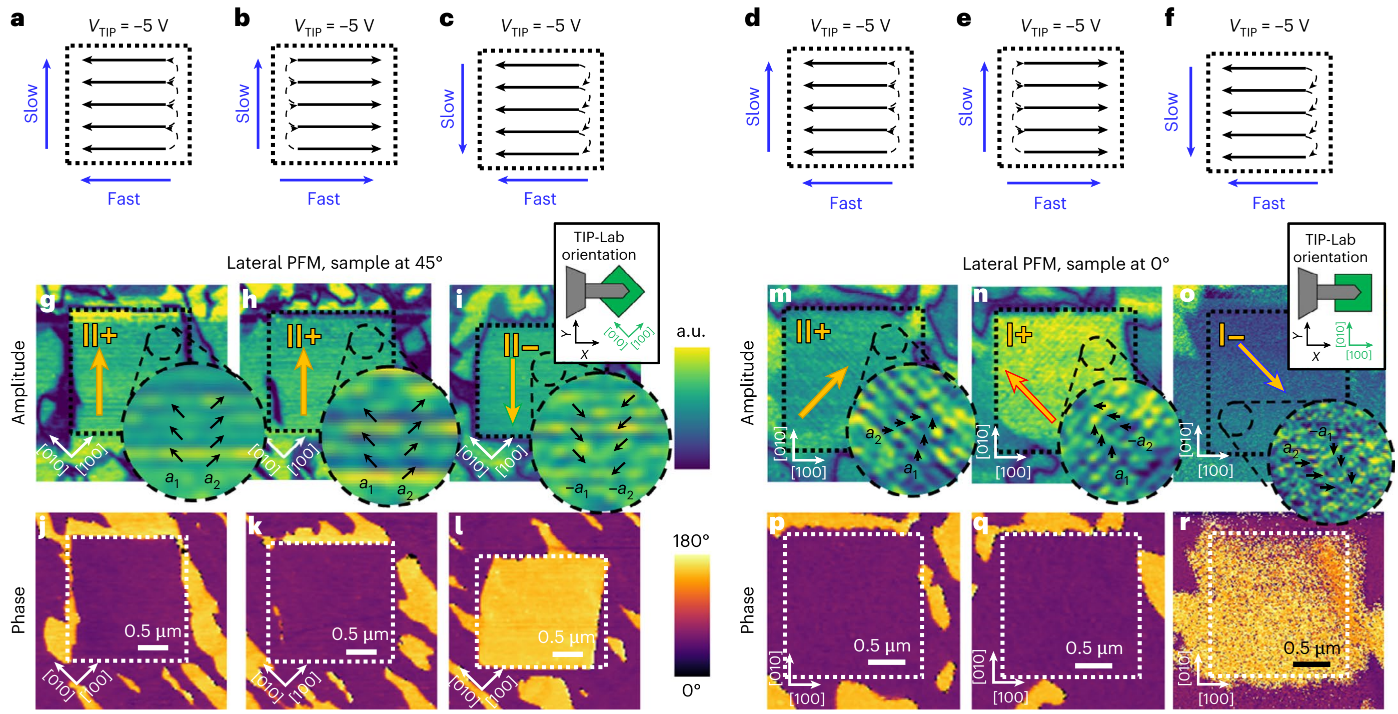

Fig. 2 | Hierarchical super-switching in PSTO. a–c, Illustration of tip bias and scan paths for different slow and fast-scan directions, respectively, with the samples' main crystallographic axis at 45° relative to the laboratory axes (*X*, *Y*). V_{TIP} is the writing bias. Inset shows the corresponding tip-laboratory orientation. **d–f**, Illustration of tip bias and scan paths for different slow and fast-scan directions, respectively, with the samples' main crystallographic axis at 0° relative to the laboratory axes (*X*, *Y*). V_{TIP} is the writing bias. Inset shows the corresponding tip-laboratory orientation, the relative orientation between the cantilever of the microscope and the axes of the laboratory. **g–l**, Lateral PFM amplitude (**g–i**) and phase (**j–l**) images post raster scanning, corresponding to the writing trajectories shown in a–c, respectively. **m–r**, Lateral PFM amplitude (**m–o**) and phase (**p–r**) images post raster-scanning, corresponding to the writing trajectories shown in **d–f**. Insets in amplitude images are amplified images to visualize the superlattice direction. The time used for the fast-scan was 1 s per line which, multiplied by 128 lines, gives us 2 min and 8 s for the slow-scan to be completed.

polarizations of the stabilized super-domain for the three different scan paths, highlighting that both the fast- and slow-scanning directions influence the super-switching, when scanning at ±45° angles relative to the pristine super-lattice stripes. Specifically, the slow-scan direction shapes the *Y*-axis polarization by aligning the a_2-domain family, while the fast-scan direction drives the *X*-axis polarization, aligning the a_1-domain family anti-parallel to the fast-scan direction and, thus, fixing a specific domain-wall orientation. This anticipates that the ferroelectric switching in this symmetry configuration is more complex than expected and probably involves a multistep process composed by several local domain rotations, governed primarily by the hierarchical ordering imposed by the material structure (Supplementary Figs. 2–4).

Thus, the super-switching process is not solely dependent on the slow-scan direction, as previously reported[30], challenging the hypothesis of a 'trailing' electric field effect. To delve into the switching mechanism, we devise strategic scan trajectories and tailored tip bias waveforms that can elucidate the intricacies of these processes, enabling the creation of targeted super-domain configurations on demand, including topological structures, such as centre convergent/divergent or flux closure.

Nanolithography of centre-convergent and centre-divergent structures

By precisely controlling the movement of the piezo-positioner during scanning, it becomes possible to guide the probe along any predetermined scan path, enabling the creation of specific topological configurations, not possible using existing scan paths (Supplementary Fig. 5). As shown in the setup sketch in (Fig. 3a), we achieved such precise control by integrating a commercially available AFM system with a field programmable gate array (FPGA), controlled externally with custom Python programs (AEcroscopy[36]). In the experiments described below, we prepare the surface via standard raster scanning with a biased tip, aligning the polarization in a specific direction over a large area (~100 μm²). This process creates a 'blank slate' in one of the four stable super-domain configurations (I−, I+, II− and II+; Supplementary Fig. 6).

For example, we demonstrate the use of a spiral-scan trajectory (Fig. 3d)—characterized by a radial slow-scan direction and tangential fast-scan motion—to nucleate and stabilize centre-convergent and centre-divergent structures using negative (Fig. 3b,c) and positive (Fig. 3e,f) tip biases, respectively. This approach unlocks the combination of the four distinct super-domain orientations into a stable configuration, with the in-plane super-domain dipoles orientated inwards and outwards, respectively, featuring charged internal (and peripheral) super-boundaries. Band-excitation lateral PFM (BE-LPFM) reveals the polarization alignment of the generated structure, finding it is not governed by the radial (slow-scanning) direction, since the super-domains are orienting the polarization anti-parallel (same direction, opposite sign) to it. As a result, super-domain alignment contrasts with expectations for raster scanning, where a parallel alignment leading to a centre-divergent structure would be expected for a negative bias scan that begins at the centre and traverses outwards radially. Instead, a centre-convergent structure is stabilized. Conversely, a positive bias, anticipated to produce a centre-convergent structure under the same scanning direction, results in a centre-divergent structure.

Interestingly, the corresponding band-excitation vertical PFM (BE-VPFM) images (Fig. 3c,f) reveal an asymmetric vertical contrast

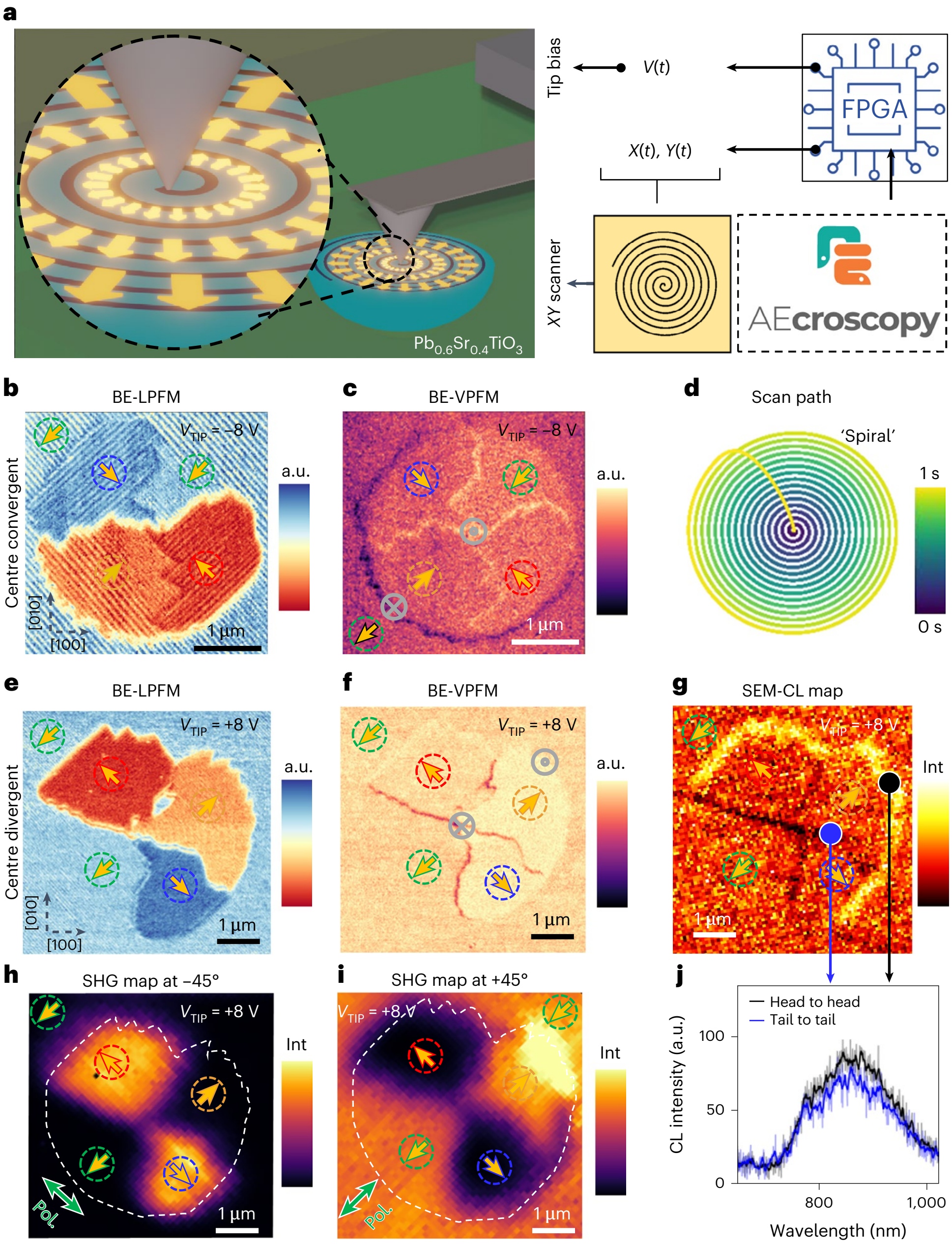

Fig. 3 | Generation of centre-divergent and centre-convergent structures through spiral-scan lithography. a, An illustration of the experimental setup used for the measurements: AEcroscopy Python package controls an FPGA, which inputs the generated signals (tip bias *V*(*t*), *X* piezo bias *X*(*t*) and *Y* piezo bias, *Y*(*t*)) to the AFM controller to autonomously perform the previously Python-designed experiment. **b**, BE-LPFM piezoresponse (cantilever long axis parallel to [100] crystallographic axis of the sample) of the written centre-convergent structure. **c**, BE-VPFM piezoresponse of the written centre-convergent structure; the grey cross and dot in a circle indicate the direction of the out-of-plane components for head to head and tail to tail. **d**, A spiral tip trajectory for the writing of the centre-convergent structure, starting the path at the centre and with a total duration of 1 s. **e**, BE-LPFM piezoresponse (cantilever long axis parallel to [100] crystallographic axis of the sample) of the written centre-divergent structure. **f**, BE-VPFM piezoresponse of the written centre-divergent structure; the grey cross and dot in a circle indicate the direction of the out-of-plane components for head to head and tail to tail. **g**, SEM-CL map of the same centre-divergent structure. **h**, An SHG map of the same centre-divergent structure with the polarizer at −45° (see green arrow). **i**, An SHG map of the same centre-divergent structure with the polarizer at +45° (see green arrow). **j**, Single SEM-CL spectra at head-to-head and tail-to-tail super-boundaries in the locations indicated by the black and blue dots in **g**, respectively. V_{TIP} is the writing bias used to generate the structure. Int, intensity of the cathodoluminescence (CL) signal.

at certain super-boundaries. Head-to-head super-boundaries exhibit a positive vertical electromechanical response, while tail-to-tail super-boundaries exhibit negative response, suggesting a local polarization tilting towards positive (and negative) out-of-plane direction at these charged locations, respectively. The lack of conductive-AFM contrast at the super-boundaries (Supplementary Fig. 7) indicates that these charges observed by KPFM are not mobile (Supplementary Fig. 8).

To explore the structural reorganization effects, we conducted correlative SHG and SEM-CL measurements on the same structures. SHG maps (Fig. 3h,i) reveal quadrant-specific excitation in centre-divergent structures, dictated by the orientation of polarized light adjusted at ±45°. This approach enables precise mapping of local polarization, complementing BE-LPFM data and providing deeper insight into generated super-boundaries. At a polarizer angle of −45° (Fig. 3h), only quadrants aligned with the incident light's polarization yield

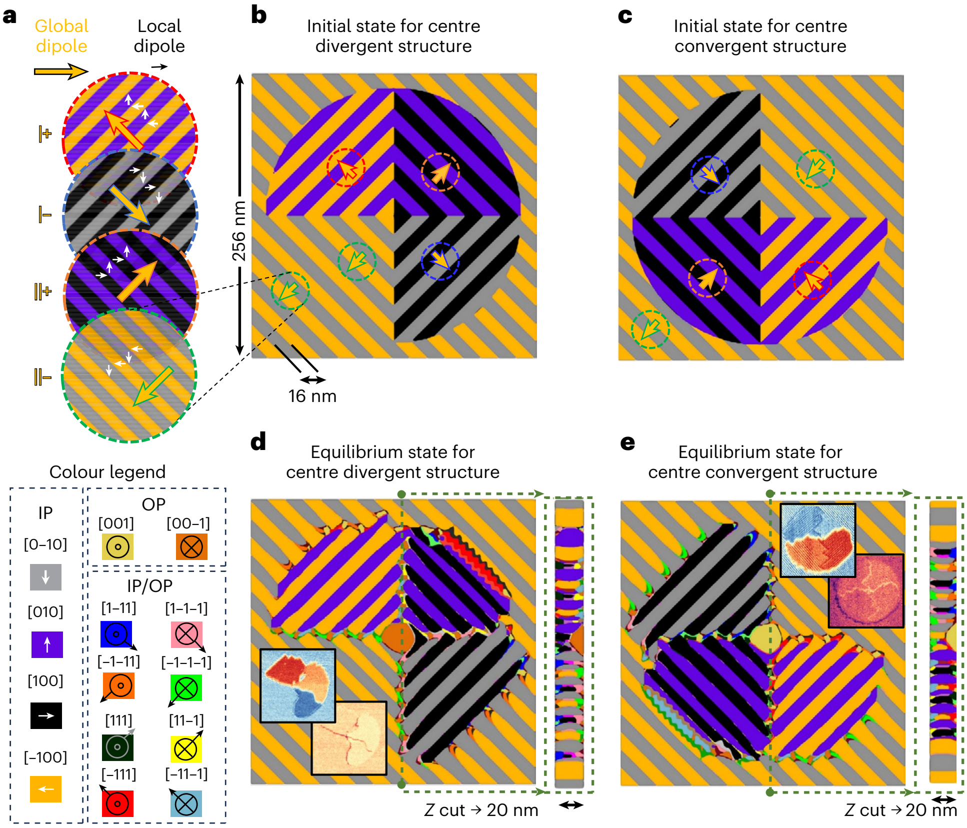

Fig. 4 | Phase-field modelling of the centre-divergent and centre-convergent structures. a, The nanoscale arrangement of the global (orange) and local (black) ferroelectric dipoles in the in-plane directions for the four different super-domains. The colour legend indicates the three-dimensional polarization direction for the phase-field structures. **b**, The initial state used in the phase-field modelling for the centre-divergent structure. **c**, The initial state used in the phase-field modelling for the centre-convergent structure. **d**, The equilibrium state obtained in the phase-field modelling for the centre divergent. The inset describes the experimental BE-LPFM and BE-VPFM of the centre-divergent structures of Fig. 3. The *Z*-cut cross-section across the whole film along the dashed green line is shown on the right. **e**, The equilibrium state obtained in the phase-field modelling for the centre-convergent. The inset describes the experimental BE-LPFM and BE-VPFM of the centre-convergent structures of Fig. 3. The *Z*-cut cross-section across the whole film along the dashed green line is shown on the right. The colour legend indicates the three-dimensional polarization direction for the phase-field structures in-plane (IP) and out-of-plane (OP).

measurable SHG signals; at +45° (Fig. 3i), complementary quadrants display SHG responses along with background. Notably, the +45° image exhibits an enhanced SHG response at head-to-head peripheral super-boundaries, indicating dipole alignment along the material's [110] axis, alongside observed out-of-plane polarization tilting.

SEM-CL measurements over the same area reveal nanoscale variations in colour centres and local polarizations (Fig. 3g), highlighting imbalanced head-to-head (bright) and tail-to-tail (dark) super-boundaries. The interaction of a focused-electron beam with a ferroelectric material is influenced by luminescent centre concentration and localized charge, shaping electron beam interactions. The near-infrared cathodoluminescence spectra peaked at 860 nm (Fig. 3j) maintains consistent shape but varies in emission intensity, suggesting changes in radiative recombination efficiency or light-emitting species concentration. In PSTO, charged defects, such as vacancies and compensating ions, are presumed to asymmetrically stabilize frustrated super-domain configurations. Positively charged head-to-head super-boundaries promote accumulation of charged defects associated with efficient light emission, resulting in stabilized luminescence that favours carrier trapping and boosts radiative recombination processes in these areas.

To deepen our understanding of the stability and polarization reorientation at the frustrated super-boundaries (Supplementary Figs. 10 and 11), we performed phase-field simulations (Fig. 4). We started with initial structures (Fig. 4b,c) mirroring the super-domain configurations observed before (Fig. 3) and, subsequently, allow these structures to relax to an equilibrium state under a tensile strain of 2% (Methods). The simulations reveal that the initial configurations indeed relax towards stable arrangements through polarization reorientation to stabilize the high electrostatic/strained super-boundary locations, which are energetically less favourable. Specifically, the tail-to-tail super-boundaries at the centre of the centre-divergent structures generate a polarization rotation towards the out-of-plane, downward direction (that is, dark orange, centre of Fig. 4d). Conversely, at the centre of the centre-convergent structure, the head-to-head super-boundaries rotate the polarization towards the out-of-plane, upward direction (that is, light green, centre of Fig. 4e), in agreement with the BE-VPFM contrast found experimentally (Fig. 3).

Likewise, in all the centre-divergent and centre-convergent structures written on a uniform 'blank slate', we find a highly frustrated peripheral super-boundary in one of the four quadrants where the super-domain of the 'blank slate' collides with the anti-parallel super-domain present in the structure (top-right super-boundary in Fig. 4c and bottom-left super-boundary in Fig. 4e). In those cases, we also observe the polarization rotation inducing an out-of-plane component of the polarization vector but in this case with additional in-plane component also present (red and light-blue walls in Fig. 4c,e, respectively), which we hypothesize is responsible for the enhanced

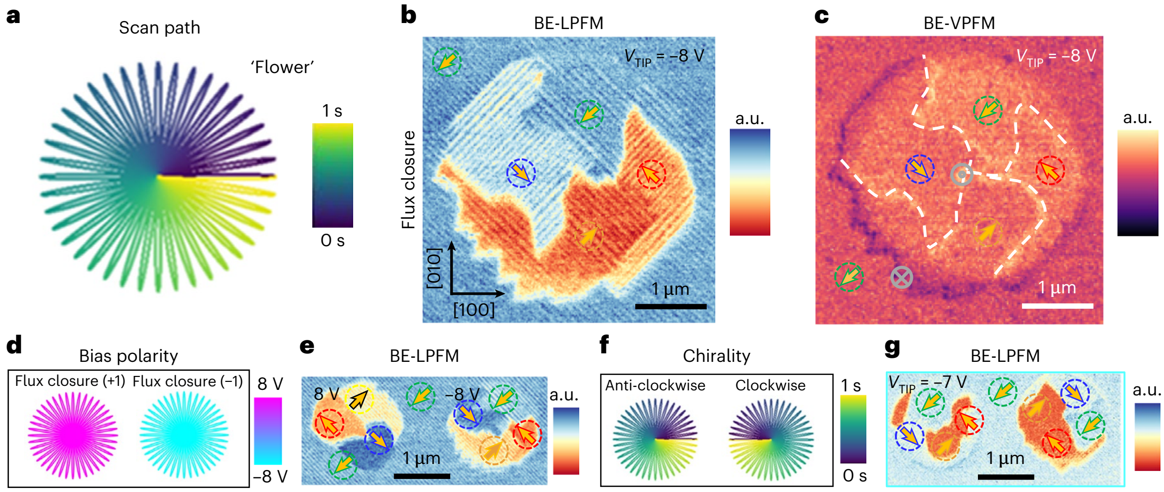

Fig. 5 | Generation of flux-closure structures through flower-scan lithography. a, Flower tip trajectory used for the writing. **b**, BE-LPFM piezoresponse (cantilever long axis parallel to [100] crystallographic axis of the sample) of the written flux-closure structure. **c**, BE-VPFM piezoresponse of the same structure; the grey cross and dot in a circle indicate the direction of the out-of-plane components for head to head and tail to tail. **d**, A scan bias polarity used to write the flux-closure states with clockwise and anti-clockwise polarization rotation. **e**, BE-LPFM piezoresponse of the structures written using the parameters in **d**. **f**, Flower scan path structure with different chirality, starting the path at the centre and with a total duration of 1 s. **g**, BE-LPFM piezoresponse of the written structures with negative bias using the scan paths in **f**. V_{TIP} is the writing bias used.

SHG signal (Fig. 3i). This reorientation also induces the formation of 'sawtooth' faceted super-boundaries to minimize the electrostatic/elastic energies (Supplementary Figs. 10 and 11). The simulations indicate that while most of the polarization arrangements are homogeneous through the thickness of the film, the small out-of-plane canting is most prominent near the film surface (cross-sections in Fig. 4c,e).

Overall, we determine that it is possible to stabilize out-of-plane polarization at the super-boundaries of PSTO through the right accumulation of elastic stress and electrostatic energy and that this material stabilizes upwards out-of-plane polarization to accommodate the head-to-head super-boundaries and, conversely, downward polarization to accommodate the tail-to-tail super-boundaries. Moreover, we suggest that indeed, the in-plane local polarization rotation steps necessary to switch the a_1/a_2 domains may happen through an intermediate out-of-plane rotation[37,38], which would be mediated by the tip vertical electric field, thus becoming the dominant agent of the in-plane super-switching (Supplementary Fig. 11).

As such, we can now revisit the hierarchical super-switching mechanism. The spiral scan starts in the central point where the vertical electric field nucleates a local out-of-plane polarization (upwards for negative bias and downwards for positive bias) surrounded by a convenient super-domain arrangement with artificial super-boundaries (head-to-head for negative bias and tail-to-tail for positive bias). In the absence of a scan path, these nucleation centres become unstable due to their small area-to-boundary ratio and quickly relax when scanned over (Supplementary Fig. 12). Spiral scanning stabilizes these centres, expanding the super-boundaries via out-of-plane intermediate switching by creating a_1/a_2 stripe domains, which are as parallel as possible to the fast-scan direction (tangential) and align appropriately with the nucleated super-domain configuration, generating a global orientation anti-parallel to the radial direction. Therefore, we speculate that in this case the stabilized final polarization arrangement is dictated by the sign of the initially nucleated domain in the centre and not by the slow-scan direction, challenging the trailing electric field theory[30,39].

Nanolithography of flux-closure structures

Next, we engineer more exotic scan paths to generate various topological states. Accordingly, we design a flower-like scan[36,40] (Fig. 5a) and explore its different permutations. The BE-LPFM of a flux-closure structure (Fig. 5b), written using a negative tip bias on a 'blank-slate' area with uniform II− super-domain, shows that it is possible to merge the four permissible super-domain orientations into a stable flux-closure structure, where in-plane dipoles rotate anti-clockwise. The corresponding BE-VPFM of the same structure (Fig. 5c) reveals vertical contrast at specific super-boundaries, akin to the centre-divergent and centre-convergent structures (that is, out-of-plane tilting upwards for head-to-head and downwards for tail-to-tail super-boundaries). Notably, the internal super-boundaries form a swirl-like shape (Fig. 5c, dashed white line) diverging from the characteristic cross-like shape typical of the centre-divergent and centre-convergent structures.

Furthermore, we prove how bias polarity determines the sign of the initial nucleation, generating anti-clockwise and clockwise flux-closure domain arrangements with positive and negative biases, respectively (Fig. 5d,e). We further explore the effect of the scan path's chirality (Fig. 5f), a mathematical concept based on a structure's distinguishability from its mirror image, critical for stabilizing polar topologies[25,41]. In this case (Fig. 5g), the slow-scan direction does modify the overall orientation of the generated structure, adding an additional degree of complexity to the stabilization of clockwise or anti-clockwise configurations.

This effect can be explained by considering all the observations of the super-switching mechanism described in previous sections and summarized elsewhere (Supplementary Fig. 13). In flower-like trajectories, the fast-scan direction is radial, promoting the growth of a_1/a_2 domains stripes radially. This symmetry is rotated by 90° with respect to the initially nucleated domain configuration; therefore, the flower-like scanning path stabilizes a structure by twisting/dragging the initially nucleated super-boundaries. Interestingly, if the chirality of the flower-scan path used during super-switching is flipped (Fig. 5g and Supplementary Fig. 13g–l), different flux-closure structures are stabilized, this time with the same bias polarity, demonstrating how handedness plays a crucial role for these chiral arrangements.

Tunability of super-domain nanoengineering

Our approach offers extensive tunability, with numerous adjustable parameters influencing nucleation and domain-dragging processes, including scan path, density, size, writing bias and duration. Leveraging an AE Python-controlled experimental setup, we can systematically

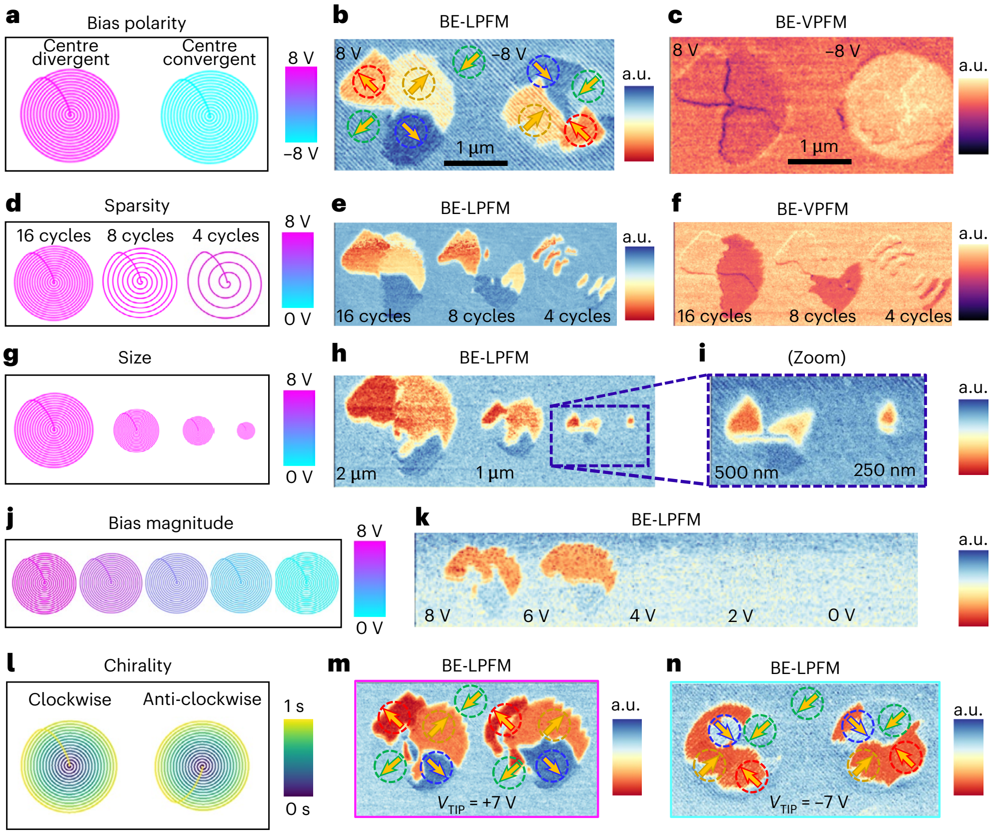

Fig. 6 | Tunability of the centre-convergent and centre-divergent states. **a**, A scan bias polarity used to write the centre-divergent and centre-convergent states. **b**,**c**, BE-LPFM piezoresponse (**b**) and BE-VPFM piezoresponse (**c**) of the structures written using the parameters in **a**. **d**, Scan paths with different sparsity. **e**,**f**, BE-LPFM piezoresponse (**e**) and BE-VPFM piezoresponse (**f**) of the structures written using the parameters in **d**. **g**, A scan path with a different size. **h**,**i**, BE-LPFM piezoresponse (**h**) and BE-VPFM piezoresponse (**i**) of the structures written using the parameters in **g**. **j**, A scan path with different writing bias magnitude. **k**, BE-LPFM piezoresponse of the structures written using the parameters in **j**. **l**, A spiral-scan path with different chirality/handedness, starting the path at the centre and with a total duration of 1 s. **m**, BE-LPFM piezoresponse of the written structures with positive bias using the scan paths in **l**. **n**, BE-LPFM piezoresponse of the written structures with negative bias using the scan paths in **l**. V_{TIP} is the writing bias used.

explore with high reproducibility (Supplementary Fig. 14) large parameter spaces in an automated fashion, enabling on-demand design and autonomous patterning of structures across the sample surface that can be subsequently read in situ using BE-PFM (Fig. 6). For example, we illustrate how bias polarity influences nucleation to produce a centre-divergent or centre-convergent structure (Fig. 6a). Subsequently, BE-LPFM (Fig. 6b) and BE-VPFM (Fig. 6c) images showcase domain structures and head-to-head and tail-to-tail super-boundary responses. Varying the tip-trajectories sparsity (Fig. 6d), with spiral paths featuring 16, 8, and 4 internal cycles, impacts the complexity and frustration of the stabilized structures (Fig. 6e,f). Exploring size dependence (Fig. 6g), with spiral sizes ranging from 2,000 nm to 250 nm (Fig. 6h), reveals stabilized structures from microns to hundreds of nanometres in radius (Fig. 6i), presumably up to where the area-to-boundary threshold for stabilization of smaller size structures is still fulfilled. Ramping writing bias magnitude (Fig. 6j), reveals a coercive voltage between 4 V and 6 V (Fig. 6k). Finally, spiral-scan trajectories in clockwise or anti-clockwise directions (Fig. 6l) reveal no effect on the stabilized structure's handedness (Fig. 6m,n).

The number of complex topologies that can be generated using this approach is not limited to the ones shown here. Supplementary Figs. 15 and 16 provide examples of shelled centre-convergent and centre-divergent structures and snake-like domains exhibiting a 'saw-tooth' polarization pattern. This work's relevance lies in understanding and manipulating super-switching using a biased AFM tip. Combining this knowledge with AE[36,40] and machine learning methods (as shown in Supplementary Figs. 17 and 18), it is possible to design and produce various complex polar topologies or optimize experimental parameters with a desired goal.

Conclusions

Our method has unveiled the intricacies of the super-switching mechanism in in-plane polarized ferroelectric films of PSTO, ruling out the 'trailing' field explanation and proposing the appearance of an intermediate out-of-plane state driven by the vertical component of the electric field. This insight has enabled the precise manipulation of super-domain structures in an on-demand fashion. Adjusting the scan path trajectory and other experimental parameters, we can create a plethora of polar topological structures, examine the delicate elastic-electrostatic energy balance and study the accommodation of frustrated super-boundaries. Furthermore, correlative microscopy techniques gather the detailed nanometric information needed to inform the phase-field models for evaluating stability and polarization reorganization. This work pioneers new nanolithography techniques for ferroics through customized tip-trajectory configurations and AE implementation, enabling the exploration of more ferroelectric topological states than previously possible.

Online content

Any methods, additional references, Nature Portfolio reporting summaries, source data, extended data, supplementary information, acknowledgements, peer review information; details of author contributions and competing interests; and statements of data and code availability are available at https://doi.org/10.1038/s41565-024-01792-1.

References

1. Chen, S. et al. Recent progress on topological structures in ferroic thin films and heterostructures. *Adv. Mater.* **33**, 2000857 (2021).
2. Catalan, G., Seidel, J., Ramesh, R. & Scott, J. F. Domain wall nanoelectronics. *Rev. Mod. Phys.* **84**, 119 (2012).
3. Marković, D., Mizrahi, A., Querlioz, D. & Grollier, J. Physics for neuromorphic computing. *Nat. Rev. Phys.* **2**, 499–510 (2020).
4. Junquera, J. et al. Topological phases in polar oxide nanostructures. *Rev. Mod. Phys.* **95**, 025001 (2023).
5. McConville, J. P. V. et al. Ferroelectric domain wall memristor. *Adv. Funct. Mater.* **30**, 2000109 (2020).
6. Seidel, J. et al. Conduction at domain walls in oxide multiferroics. *Nat. Mater.* **8**, 229–234 (2009).
7. Luk'yanchuk, I., Tikhonov, Y., Razumnaya, A. & Vinokur, V. M. Hopfions emerge in ferroelectrics. *Nat. Commun.* **11**, 2433 (2020).
8. Wang, J. et al. Polar Solomon rings in ferroelectric nanocrystals. *Nat. Commun.* **14**, 3941 (2023).
9. Balke, N. et al. Deterministic control of ferroelastic switching in multiferroic materials. *Nat. Nanotechnol.* **4**, 868–875 (2009).
10. Balke, N. et al. Enhanced electric conductivity at ferroelectric vortex cores in $BiFeO_3$. *Nat. Phys.* **8**, 81–88 (2012).
11. Winkler, R. S. et al. Electromechanical manipulation of topological defects to yield giant piezoelectric response in epitaxial lead zirconate titanate bilayers on silicon. *Adv. Electron. Mater.* **7**, 2100195 (2021).
12. Das, S. et al. Observation of room-temperature polar skyrmions. *Nature* **568**, 368–372 (2019).
13. Zhang, H.-Y. et al. Observation of vortex domains in a two-dimensional lead iodide perovskite ferroelectric. *JACS* **142**, 4925–4931 (2020).
14. Yadav, A. K. et al. Observation of polar vortices in oxide superlattices. *Nature* **530**, 198–201 (2016).
15. Gradauskaite, E. et al. Defeating depolarizing fields with artificial flux closure in ultrathin ferroelectrics. *Nat. Mater.* https://doi.org/10.1038/s41563-023-01674-2 (2023).
16. Han, L. et al. High-density switchable skyrmion-like polar nanodomains integrated on silicon. *Nature* **603**, 63–67 (2022).
17. Tang, Y. L. et al. Observation of a periodic array of flux-closure quadrants in strained ferroelectric $PbTiO_3$ films. *Science* **348**, 547–551 (2015).
18. Wang, Y. J. et al. Polar meron lattice in strained oxide ferroelectrics. *Nat. Mater.* **19**, 881–886 (2020).
19. Sánchez-Santolino, G. et al. A 2D ferroelectric vortex pattern in twisted $BaTiO_3$ freestanding layers. *Nature* **626**, 529–534 (2024).
20. Ma, J. et al. Controllable conductive readout in self-assembled, topologically confined ferroelectric domain walls. *Nat. Nanotechnol.* **13**, 947–952 (2018).
21. Yang, W. et al. Quasi-one-dimensional metallic conduction channels in exotic ferroelectric topological defects. *Nat. Commun.* **12**, 1306 (2021).
22. Vasudevan, R. K. et al. Exploring topological defects in epitaxial $BiFeO_3$ thin films. *ACS Nano* **5**, 879–887 (2011).
23. Gao, Z. et al. Mechanical manipulation for ordered topological defects. *Sci. Adv.* **10**, eadi5894 (2024).
24. Guo, M. et al. Electrically and mechanically driven rotation of polar spirals in a relaxor ferroelectric polymer. *Nat. Commun.* **15**, 348 (2024).
25. Shao, Y.-T. et al. Emergent chirality in a polar meron to skyrmion phase transition. *Nat. Commun.* **14**, 1355 (2023).
26. Wu, H. et al. Magnetic memory driven by topological insulators. *Nat. Commun.* **12**, 6251 (2021).
27. Domingo, N. Bowing to ferroelectric artificial flux closure. *Nat. Mater.* **22**, 1441–1443 (2023).
28. Scott, J. F. et al. Superdomain dynamics in ferroelectric-ferroelastic films: switching, jamming, and relaxation. *Appl. Phys. Rev.* **4**, 041104 (2017).
29. McQuaid, R. G., Gruverman, A., Scott, J. F. & Gregg, J. M. Exploring vertex interactions in ferroelectric flux-closure domains. *Nano Lett.* **14**, 4230–4237 (2014).
30. Matzen, S. et al. Super switching and control of in-plane ferroelectric nanodomains in strained thin films. *Nat. Commun.* **5**, 4415 (2014).
31. Kavle, P. et al. Strain-driven mixed-phase domain architectures and topological transitions in $Pb_{1-x}Sr_xTiO_3$ thin films. *Adv. Mater.* **34**, 2203469 (2022).
32. Kavle, P. et al. Exchange-interaction-like behavior in ferroelectric bilayers. *Adv. Mater.* **35**, 2301934 (2023).
33. Chen, C. et al. Deterministic manipulation of multi-state polarization switching in multiferroic thin films. *Adv. Funct. Mater.* **33**, 2208244 (2023).
34. Kelley, K. P. et al. Probing metastable domain dynamics via automated experimentation in piezoresponse force microscopy. *ACS Nano* **15**, 15096–15103 (2021).
35. Wu, M. et al. Facile control of ferroelastic domain patterns in multiferroic thin films by a scanning tip bias. *ACS Appl. Mater. Interfaces* **15**, 11983–11993 (2023).
36. Liu, Y. et al. AEcroscopy: a software–hardware framework empowering microscopy toward automated and autonomous experimentation. *Small Methods* (2024); https://doi.org/10.1002/smtd.202301740
37. Fedorova, N. S. et al. Understanding magnetoelectric switching in $BiFeO_3$ thin films. *Phys. Rev. B* **109**, 085116 (2024).
38. Heron, J. T. et al. Deterministic switching of ferromagnetism at room temperature using an electric field. *Nature* **516**, 370–373 (2014).
39. Wu, M. et al. Complete selective switching of ferroelastic domain stripes in multiferroic thin films by tip scanning. *Adv. Electron. Mater.* (2024); https://doi.org/10.1002/aelm.202300640
40. Liu, Y., Checa, M. & Vasudevan, R. K. Synergizing human expertise and AI efficiency with language model for microscopy operation and automated experiment design*. *Mach. Learn. Sci. Technol.* **5**, 02LT01 (2024).
41. Behera, P. et al. Electric field control of chirality. *Sci. Adv.* **8**, eabj8030 (2022).

Methods

Sample preparation

The films studied in this work were produced with pulsed-laser deposition using a KrF excimer laser (248 nm, LPX 300, Coherent), such as in ref. 34. The work here focuses on heterostructures of the form 100 nm PSTO/30 nm $SrRuO_3$/$DyScO_3$(110) (CrysTec GmbH) using established procedures[31,32]. The $SrRuO_3$ growth was carried out first at a heater temperature of 690 °C in a dynamic oxygen pressure of 100 mTorr with a laser fluence of 1 J cm^{-2} and a laser repetition rate of 17 Hz from a ceramic target (Praxair) of the same composition. Following that growth, the PSTO growth was carried out at a heater temperature of 625 °C in a dynamic oxygen pressure of 200 mTorr with a laser fluence of 1.9 J cm^{-2}. The laser repetition rates of 10 and 2 Hz were used for the $Pb_{1.1}TiO_3$ ceramic target (Praxair) and the $SrTiO_3$ single-crystal target, respectively. The desired composition was achieved via subunit cell-level material mixing using the synchronized targets motion and laser pulse sequence. The 10% excess lead in the $Pb_{1.1}TiO_3$ target was found to be vital to compensate the lead loss during growth. Following the growth, the samples were cooled to room temperature at 10 °C min^{-1} in a static oxygen pressure of 700 Torr. The as-grown films were also characterized by X-ray diffraction including symmetric θ–2θ line scans, rocking curves and two-dimensional reciprocal space mapping studies using a high-resolution X-ray diffraction X'pert Pro2, PANalytical system (Supplementary Fig. 19). All films studied herein were found to be highly crystalline and fully epitaxial.

Writing the topological structures

Arbitrary path scanning of the AFM probe is accomplished by employing a Cypher AFM system (from Asylum Research, an Oxford Instruments company) controlled through an FPGA using a custom LabVIEW/Python interface. This interface directs the tip's movement along any desired trajectory by inputing the desired waveforms directly to the *XY* piezoscanners of the commercial AFM (Supplementary Fig. 4 and other works[42,43]). The tips utilized are commercially available Multi75-G (BudgetSensors) with a free resonance frequency of 75 kHz and a spring constant of 3 N m^{-1}.

Reading the topological structures

BE-PFM was performed using external data acquisition electronics based on a NI-6115 fast DAQ card controlled by custom-built LabVIEW software[44]. A chirp voltage signal around the first cantilever contact resonance frequency (~350 kHz) or the torsional contact resonance frequency (~650 kHz) was applied to the AFM probe while the sample was grounded, for vertical and lateral polarization reading, respectively. The PFM experimental data were stored in h5 files and post-processed using the Python pycroscopy package[45]. LPFM images at orthogonal cantilever orientations are shown in Supplementary Fig. 20, where the different in-plane components can be studied for the same area of the sample.

Phase-field simulations

To perform the phase-field simulations, we selected $PbTiO_3$ as a ferroelectric thin film for our model. We employed a polarization vector $P_i = (P_x, P_y, P_z)$ as an order parameter to denote the state of polarization along the *x*, *y* and *z* directions (P_x, P_y and P_z) in the global coordinates system. The total free energy density of the system can be expressed by

$$F = \int_V \{f_{\mathrm{grad}}(P_{i,j}) + f_{\mathrm{bulk}}(P_i) + f_{\mathrm{elec}}(P_i, E_i) + f_{\mathrm{elas}}(P_i, \varepsilon_{ij})\} \mathrm{d}V, \qquad (1)$$

where f_{elas}, f_{grad}, f_{bulk} and f_{elec} denote elastic energy, gradient energy, bulk energy and electrostatic energy, respectively. V is the total volume of the system. E_i and ε_{ij} are the components of the electric field and elastic strain, respectively. A detailed explanation of each energy density in equation (1) can be found in literature[46].

The temporal evolution of the polarization vector P_i is calculated by solving the time-dependent Landau–Ginzburg–Devonshire equation:

$$\frac{\partial P_i(x,t)}{\partial t} = -L\frac{\partial F}{\partial P_i(x,t)}, (i = 1-3), \qquad (2)$$

where t is time, x is the spatial position and L is a kinetic coefficient related to the mobility of the domain wall.

The simulation was done using a realistic three-dimensional geometry and the system size was chosen to be $256\Delta x \times 256\Delta y \times 32\Delta z$, with $\Delta x = \Delta y = \Delta z = 1\,\mathrm{nm}$. The thickness of the substrate, air and film are 10 nm, 2 nm and 20 nm, respectively. The substrate strain was set at 2% to stabilize the structure properly, and the simulation was performed at room temperature. The periodic boundary conditions were applied along in-plane directions (*x* and *y*), whereas proper mechanical and electrical boundary conditions were applied along out-of-plane (*z*) directions. The isotropic relative dielectric coefficient k_{ii} is set to be 50, while the gradient energy coefficients are chosen to be $\frac{G_{11}}{G_{110}} = 0.6$, where $G_{110} = 1.73 \times 10^{-10}\,\mathrm{C^{-2}\,m^4\,N^{-1}}$. Other constants, such as Landau coefficients, elastic compliance and electrostrictive coefficients, are taken from literature[47].

SHG

In the SHG, a linearly polarized laser light at a frequency ω is focused onto the sample, and the reflected light at the frequency 2ω is detected accounting for the nonlinear light–matter interactions occurring in non-centrosymmetric materials. By raster scanning the excitation laser and collecting spectra at each location, spatial maps of the polarization orientation relative to the incident excitation polarization can be obtained. The SHG measurements were conducted using a 100 fs Ti:sapphire laser (Mai Tai HP, Spectra Physics) at 800 nm and 80 MHz repetition rate. The laser beam was passed through a half-wave plate mounted in a rotation stage and was directed into an upright microscope (Olympus) and focused onto a sample surface using a 100× microscope objective (numerical aperture 0.9) to a ~1.1-µm-diameter spot. The laser energy at the sample surface was 0.8 mW. The SHG light was collected in backscattering configuration using the same objective and was directed to a monochromator (Spectra Pro 2300i, Acton, *f* = 0.3 m) that was coupled to the microscope and equipped with a 150 grooves per millimetre grating and a charge-couple device (CCD) camera (Pixis 256BR, Princeton Instruments). Before entering the monochromator, the SHG light was passed through a short-pass cut-off filter (650 nm) to filter out the fundamental excitation light at 800 nm and a polarizer to select SHG polarization colinear or cross relative to the polarization of the excitation light[48]. A motorized computer-controlled *XY* microscope stage (Marzhauser) with minimum scanning steps of 100 nm was used to perform SHG mapping. Polarization-resolved measurements were performed by inserting a computer-controlled rotational stage with a broad-band half-wave plate into excitation and back-scattered SHG beam paths.

SEM-CL

Cathodoluminescence spectra were obtained using an FEI Quattro environmental SEM equipped with a Delmic Sparc cathodoluminescence collection module. This setup enabled concurrent acquisition of secondary electron signals and cathodoluminescence spectra for spatially resolved analyses. The measurements were performed with an electron accelerating voltage of 5 kV and a beam current of 230 pA over a square scan area of 7.2 × 7.2 µm^2 with a chosen pixel density of 125 × 125.

Data availability

The data that support the findings of this study are available from the corresponding author upon request.

Code availability

Python scripts used for the analysis are available in Github at https://github.com/mchecanu/Topological_ferroelectrics and Zenodo at https://doi.org/10.5281/zenodo.10728429 (ref. 49).

References

42. Checa, M. et al. High-speed mapping of surface charge dynamics using sparse scanning Kelvin probe force microscopy. *Nat. Commun.* **14**, 7196 (2023).
43. Checa, M., Kelley, K., Vasudevan, R., Collins, L. & Jesse, S. Automated piezoresponse force microscopy domain tracking during fast thermally stimulated phase transition in CuInP2S6. *Nanotechnology* **34**, 325703 (2023).
44. Peters, T., Zhu, W., Checa, M., Collins, L. & Trolier-McKinstry, S. Influence of doping and thickness on domain avalanches in lead zirconate titanate thin films. *Appl. Phys. Lett.* https://doi.org/10.1063/5.0149457 (2023).
45. Somnath, S., Smith, C. R., Laanait, N., Vasudevan, R. K. & Jesse, S. USID and Pycroscopy—open source frameworks for storing and analyzing imaging and spectroscopy data. *Microsc. Microanal.* **25**, 220–221 (2019).
46. Zhang, H. et al. Strain phase diagram and physical properties of (110)-oriented $PbTiO_3$ thin films by phase-field simulations. *Acta Mater.* **228**, 117761 (2022).
47. Haun, M. J., Furman, E., Jang, S., McKinstry, H. & Cross, L. Thermodynamic theory of $PbTiO_3$. *J. Appl. Phys.* **62**, 3331–3338 (1987).
48. Vlassiouk, I. et al. Armor for steel: facile synthesis of hexagonal boron nitride films on various substrates. *Adv. Mater. Interfaces* **11**, 2470001 (2024).
49. Checa, M. mchecanu/Topological_ferroelectrics: topological_ferroelectrics (topological_ferroelectrics). *Zenodo* https://doi.org/10.5281/zenodo.10728429 (2024).

Acknowledgements

Research was supported by the Center for Nanophase Materials Sciences, which is a US Department of Energy, Office of Science User Facility at Oak Ridge National Laboratory. The cathodoluminescence research was supported by the US Department of Energy, Office of Science, Office of Basic Energy Sciences Energy Frontier Research Centers program under Award Number DE-SC0021118. P.K. acknowledges the support of the Army Research Office under the ETHOS MURI via cooperative agreement W911NF-21-2-0162 and the Intel Corp. via the COFEEE programme. A.D. acknowledges the support of the National Science Foundation via Grant DMR-2102895. L.W.M. acknowledges the support of the National Science Foundation via Grant DMR-2329111. Y.C. acknowledges the support of the National Science Foundation via Grant CMMI-2132105.

Author contributions

M.C., K.K. and N.D. conceived the research. M.C. designed and performed the writing of the structures and PFM measurements. A.P. performed the SHG measurements. B.D. performed the SEM-CL measurements. B.P. and Y.C. performed the phase-field modelling. S.J. built the LabVIEW code needed to interconnect the Python interface with the AFM. R.K.V. assisted in the Python coding and interpretation of the results. Y.L. performed the Gaussian process optimization. P.K., A.D. and L.W.M. performed the sample growth and preparation. K.P.K., L.C., R.K.V. and N.D. provided experimental support and helped in the interpretation of the results. M.C. prepared the figures and wrote the manuscript with support of all the co-authors.

Competing interests

The authors declare no competing interests.

Additional information

Supplementary information The online version contains supplementary material available at https://doi.org/10.1038/s41565-024-01792-1.

Correspondence and requests for materials should be addressed to Marti Checa.

Peer review information *Nature Nanotechnology* thanks Weijin Chen, Ignasi Fina and Pavan Nukala for their contribution to the peer review of this work.